

Aerodynamic characterisation of porous fairings : pressure drop and Laser Doppler Velocimetry measurements

Fabien Méry^{1,*} and Delphine Sebbane¹

¹ONERA, Université Fédérale de Toulouse, Toulouse, France

*corresponding author(s): Fabien Méry (fabien.mery@onera.fr)

ABSTRACT

The present data descriptor presents the pressure drop measurements and the steady and unsteady velocity flow field through fairing samples in the B2A test bench measured by Laser Doppler Velocimetry.

Background & Summary

Aviation has become a mass transportation industry, and all prospective studies foresee growth in this sector. Among the challenges, noise in the vicinity of airports has gone from a marginal annoyance to a real public health concern. To address this problem, as well as others such as fuel consumption, aircraft manufacturers are considering radically new aircraft architectures that could enter service quickly. In the meantime, however, the noise of traditional aircraft must be reduced significantly. Aircraft noise, during takeoff and landing, results primarily from a combination of (i) engine noise, which is generated by the fan and jet, and (ii) airframe noise, primarily due to the landing gear (LG) and high lift devices (HLD), the latter including slats and trailing edge flaps, which are deployed at low speeds to increase lift. During takeoff, engine noise remains dominant, while on approach and landing, engines operate at low speeds (typically 50% of N1), and airframe noise becomes a significant contributor, especially for newer aircraft equipped with latest generation turbofans. Its mitigation is therefore of primary interest. However, due to the strong integration constraints imposed by other disciplines than acoustics on components such as LGs and HLDs, the development of noise reduction technologies (NRT) on these airframe components has been limited. This lack of breakthroughs is also due to the complexity of flow physics, and thus our still limited knowledge of airframe noise generation mechanisms. The noise of the landing gear, slats and flaps has been studied on a real and reduced scale, mainly on the basis of experimental means. The maturity of numerical simulations now allows to study the mechanisms of the noise sources on various complex configurations. Moreover, numerical simulation methods can be sufficiently accurate to predict the noise generated by such configurations. In order to take the next step in the maturity of numerical prediction, these NRTs must be accurately evaluated and modeled. Experimental data based on academic configurations are therefore needed to validate the new tools and numerical models.

One promising NRT is the use of a fairing in front of the landing gear to reduce the noise of this system¹. The present study aims at collecting an experimental database (pressure drop and turbulence characteristics) of several fairing solutions in order to have validation test cases for CFD simulation and thus develop new models for such complex geometries. The fairing samples are thus tested on the "Acoustic and Aerothermal Bench" (B2A), by measuring the pressure drop of each sample and the flow field by Laser Doppler Velocimetry (LDV). The experimental methodology will be presented first. The database will then be described. Some technical validations will also be proposed on the basis of a comparison with the literature.

Methods

Test rig, Set-up and instrumentation

The aeroacoustic test bench (B2A)² at ONERA is made of a stainless steel tube of section 50×50 mm; its total length is about 4 m. A 0.2-m-long test section is equipped with two silica windows for optical access. The termination is equipped with a quasi-anechoic outlet, leading to an upstream reflection coefficient smaller than 0.2 for frequencies higher than 500 Hz. A mean flow with a bulk Mach number M_b up to 0.5 can be provided. The static flow temperature can be accurately regulated from the ambient temperature up to 300°C. In the test section, this flow shows fully developed turbulent boundary layers, with a turbulence rate of a few percent at the center of the test section. As shown in Figure 1, flow propagates from left to right. The test bench is connected to a pressurized air tank. A mass flow control valve can regulate the mass flow with a high

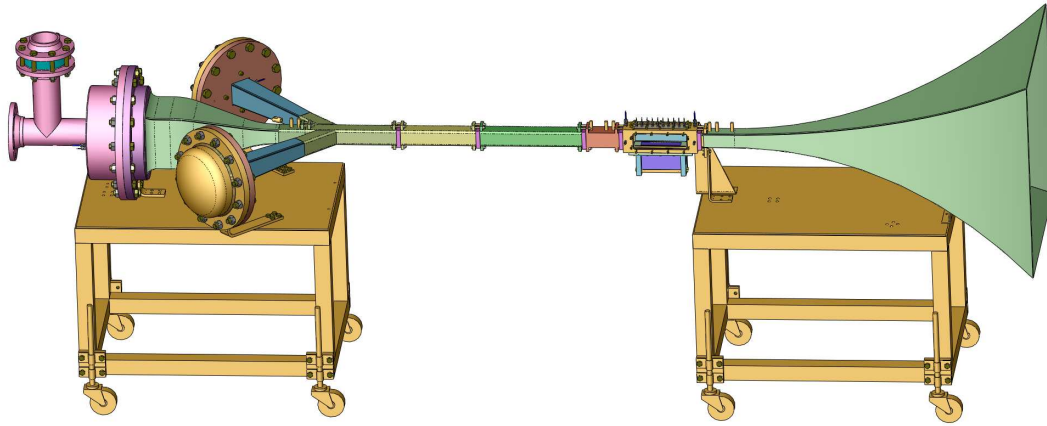


Figure 1. B2A test rig

Pressure label	PS1	PS2	PS3	PS4	PS5	PS6	PS7
Streamwise position [mm]	0	15	30	45	60	75	215

Table 1. Pressure taps position

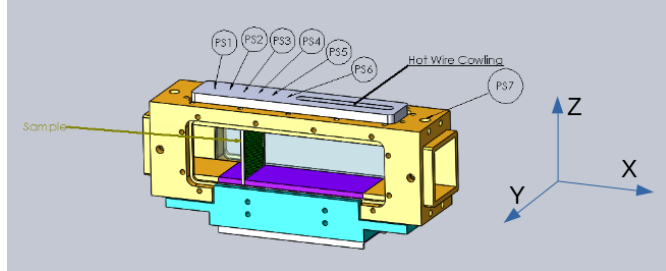
43 accuracy (less than 1% error on the imposed mass flow rate). This mass flow rate is measured with a flow meter (Rosemount
 44 485 Annubar) installed on the mass flow control valve. It ranges from 50g/s up to 500g/s. The bulk Mach number can be thus
 45 derived from the mass flow definition.

46 Figure 2a presents an overview of the experimental setup. The fairing sample is placed across the test section and covers all
 47 its cross-sectional area. Static pressure taps are available on the top of the test section upstream and downstream the sample.
 48 Tab 1 gives the position of the pressure taps (PS1 is the reference). The sample is placed 37.5mm downstream the PS1 pressure
 49 tap. The static pressures are monitored and acquired using the SVMTec differential pressure scanner. The scanner has a
 50 1.250kPa range with an uncertainty of max +/-0.1% of the full scale span. The sampling rate is 10Hz and 200 samples are
 51 acquired. The reference pressure tap PS1 is also measured by a 45 Psi Digiquartz absolute pressure sensor in order to have the
 52 absolute static pressure upstream to the sample. The sampling rate is 4Hz and 80 samples are acquired. When the SVMtec
 53 scanner is out of range for high pressure drop samples, only the Digiquartz sensor is used on all the pressure taps.

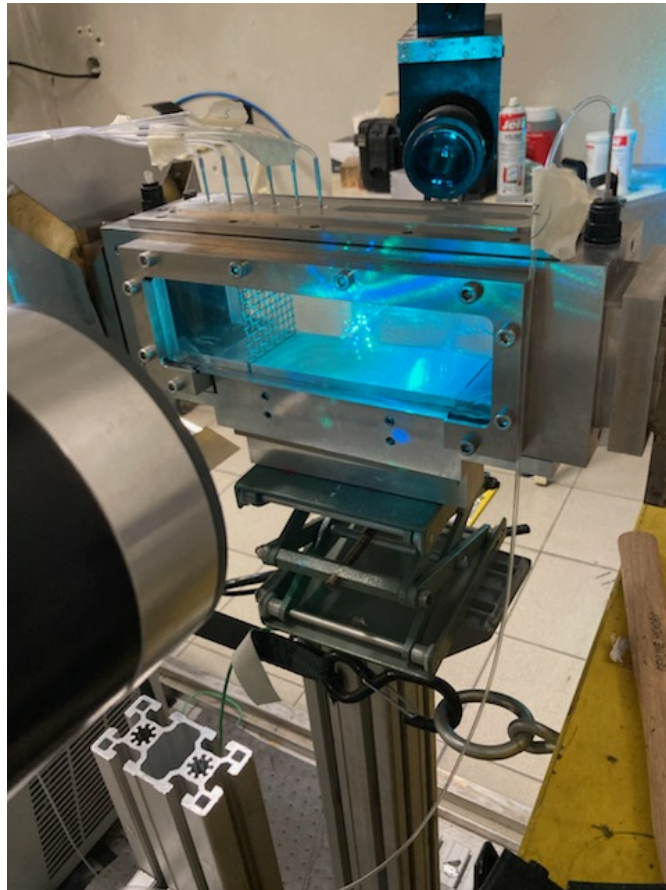
54 A two-component fringe-mode LDV allows the measurement of the axial U and vertical W velocity components in almost
 55 the entire volume of the test section³. The emitting optics produce an elliptical measurement volume whose little axis can be as
 56 small as 50 microns. Flow is seeded with amorphous silica particles. The LDV signal is unevenly sampled due to the random
 57 arrival of particles in the measurement volume. A reconstruction method^{2,4} is used to resample the raw data at a constant rate.
 58 Signals are processed using the in-house ONERA software, ASSA⁵. A minimum sampling rate of $f_m = 15kHz$ measurements
 59 per second is ensured, for each velocity component, and more than 200,000 samples are acquired so that statistical convergence
 60 of the mean velocity is largely ensured. Figure 2 shows an on going measurement. The U and W components are measured for
 61 4 (X,Y) planes. Each planes are composed of a regular grid of 6X6 points (36 points). Each grid dimension is 25mmX25mm
 62 centered in the test section. The first plane is measured upstream the sample (12mm upstream the sample) and the 3 other
 63 planes are positioned downstream the sample (35mm, 81mm and 128 mm).

64 Sample description

65 The samples are adapted to fit in the B2A test section: the samples cover the whole cross-test section surface. Tabs 2, 3 and 4
 66 show the tested samples with their label and the measurements performed on each one. The SCP **DaTbec** types are perforated
 67 panels: a represents the hole diameter in mm, b represents the distance between holes in mm and c the material thickness in
 68 mm. The angle Φ represents the angle of the perforations (one sample only with this feature). The WM Videfil4 is a classical
 69 grid (LT type⁶). The wire diameter is d and M is the mesh width: in the present case, $M = 5mm$ and $d = 1mm$. The porosity of
 70 such a sample writes $\sigma = (1 - \frac{d}{M})^2 = 0.64$. The TU Delft sample is a sample where a 3D model is reproduced along the test
 71 section dimension. The template shape and the geometric characteristics are shown in figure 3.



(a) B2A INVENTOR Test section. The fairing sample is located inside the test section, perpendicular to the flow.



(b) LDV measurement on going

Figure 2. B2A setup for INVENTOR activity

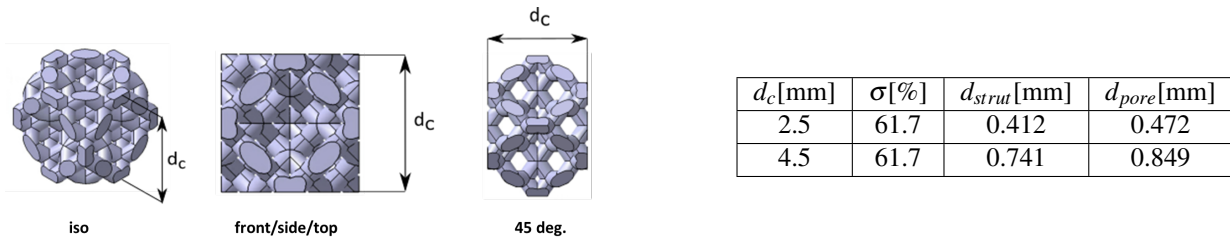


Figure 3. Diamond grid model and characteristics

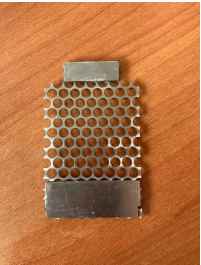
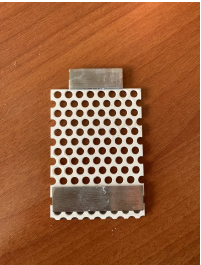
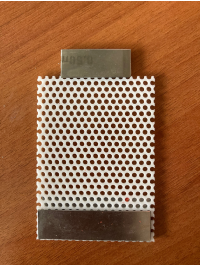

Description of the sample		Measurements	
Sample label	Picture	Pressure	LDV
SCP D5T6e1		X	
SCP D4T6e1		X	
SCP D2T3e2		X	X
SCP D2T3e1		X	

Table 2. Sample description (a)

⁷² **Pressure drop post-processing procedure**

The pressure drop coefficient is defined by :

$$\xi = \frac{\Delta P_i}{\frac{\gamma}{2} P_0 M^2} \quad (1)$$

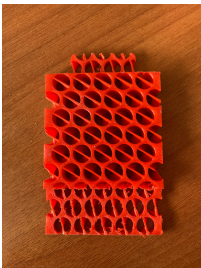
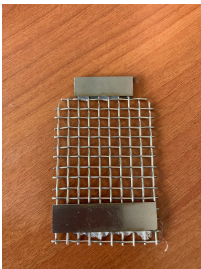


Description of the sample		Measurements	
Sample label	Picture	Pressure	LDV
HP		X	
WM Vide4Fil1		X	X
WM DLR		X	
OPAL D2T3.2Phi30e1		X	

Table 3. Sample description (b)

The mass flow is regulated in the B2A bench and it is assumed that we are in incompressible conditions. The pressure drop coefficient or resistance coefficient writes thus:

$$\xi = \frac{\Delta P_s}{\frac{\gamma}{2} P_0 M_b^2} \quad (2)$$

73 Indeed, the total pressure drop ΔP_t is equivalent to the static pressure drop ΔP_s . M_b is the bulk Mach number of the test bench
74 derived from the measured mass flow and the temperature is assigned and regulated. The Morgan's method⁷ is applied to
75 assess the value of ΔP_s . This method was also used by Pinker and Herbert⁸. The idea is to use several pressure taps and to
76 retrieve the pressure loss due to the friction loss inside the duct so that only the pressure drop due to the sample is extracted.
77 Figure 4 illustrate the principle of the method applied to the WM Vide4Fil sample. For each flow condition, the post-processing
78 proposed by Morgan enables to extract only the pressure drop contribution coming from the sample. This procedure is applied
79 to each sample in order to ensure accurate assessment of the induced pressure drop.


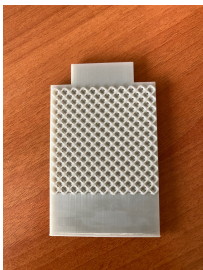
Description of the sample		Measurements	
Sample label	Picture	Pressure	LDV
TU delft diamond $d_c = 2.5\text{mm}$		X	
TU delft diamond $d_c = 4.5\text{mm}$		X	X

Table 4. Sample description (c)

80 Data records

81 The full data set is available on zenodo deposit (10.5281/zenodo.7052546).

Mass flow [g/s]	50	75	106
Bulk velocity [m/s]	17	25	36
Reynolds number based on the B2A dimensions	55000	83000	117000

Table 5. Flow conditions at 20°C

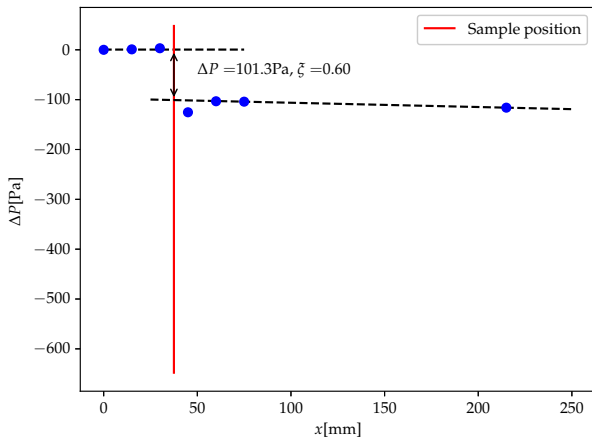
82 Table 5 recalls the flow condition performed during this study and the corresponding Reynolds number based on the B2A
83 test section width.

84 Pressure drop results

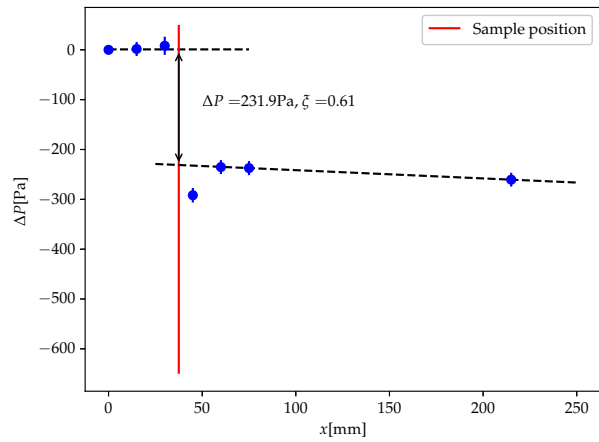
85 The pressure drop data record is composed of a csv file called "pressure_drop.csv". The results are summarized in Table 6.

Mass flow [g/s]	50	75	106
Bulk velocity [m/s]	17	25	36
WM Vide4Fil1	0.60	0.61	0.61
SCP D5T6e1	1.21	1.24	1.17
SCP D4T6e1	3.27	3.35	3.22
SCP D2T3e2	2.88	2.60	2.70
SCP D2T3e1	5.03	5.16	5.16
HP	4.13	4.51	4.41
OPAL D2T3.2Phi30e1	13.45	13.99	14.99
Diamond Grids 2.5mm	110.4	117.5	177.6
Diamond Grids 4.5mm	62.2	65.6	70.77
WM DLR	56.88	54.54	56.36

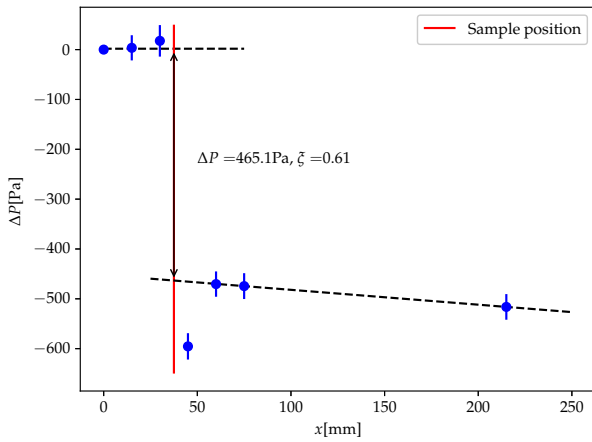
Table 6. Overall pressure drop coefficient ξ results



(a) $V_b = 17\text{m/s}$



(b) $V_b = 25\text{m/s}$



(c) $V_b = 33\text{m/s}$

Figure 4. Pressure drop measurement procedure. the differential static pressure measured at each pressure tap with reference to the most upstream one is plotted in blue circle. The pressure drop induced by the sample is assessed from the delta between the two black dashed lines values at the sample position.

86 **LDV results**

87 The LDV data records are of two types : statistical results on the velocity field and binary results, which include the time
88 evolution of the measured instantaneous velocity (with roughly 200,000 time samples for each measurement point).

Mass flow [g/s]	50	75	106
Bulk velocity [m/s]	17	25	36
WM Vide4Fil1	Stats_wmon_50gs_en.dat	Stats_wmon_75gs_en.dat	Stats_wmon_106gs_en.dat
SCP D2T3e2	Stats_scp_50gs_en.dat	Stats_scp_75gs_en.dat	Stats_scp_106gs_en.dat
Diamond Grids 4.5mm	Stats_tud_50gs_en.dat	Stats_tud_75gs_en.dat	-

Table 7. Data record file name for statistical results

89 Each file "Stats_yyy_xxgs_en.dat" is a tecplot format compatible file. The variables can be described as followed:

- 90 • "Point", Number of point which corresponds to the point label for the binary file
91 • X, Y, Z, Coordinates in [mm]

Mass flow [g/s]	50	75	106
Bulk velocity [m/s]	17	25	36
WM Vide4Fil1	WMON1	WMON2	WMON3
SCP D2T3e2	SCP1	SCP2	SCP3
Diamond Grids 4.5mm	TUD1	TUD2	-

Table 8. Data record binary path for unsteady velocity results

- 92 • U, W , Mean value of the velocity in [m/s]
- 93 • $SdevU, SdevW$, Standard deviation of the velocity
- 94 • $VarU, VarW$, Variance of the velocity component
- 95 • SkU, SkW , Skewness of the velocity component
- 96 • FIU, FIW , Flatness of the velocity component
- 97 • UW , Cross correlated momentum

98 Table 8 presents the path for the binary files and which flow conditions they are corresponding to.

99 The binary results are named "INVE0XXX.bin". The program "PSD_estimation.py" gives some routines to read and
100 calculate the PSD of a given velocity component and a given point.

101 Technical validation

102 Wiremesh pressure drop analysis

For an incompressible flow, ξ is only a function of the porosity of the screen and the Reynolds number based on the wire diameter⁹. It has been shown that the pressure resistance coefficient can be approximated as⁸:

$$\xi = f(Re_d) \frac{1 - \beta^2}{\beta^2} \quad (3)$$

103 where f is a decaying function of Re_d , which is the Reynolds number based on the wire diameter. Roach¹⁰ suggests to use
104 $f = 0.52 + 66Re_d^{-4/3}$ while Groth and Johansson¹¹ propose $f = 0.4 + 8.4Re_d^{-4/5}$. In the Re_d interval $40 - 10^5$, f decays as
105 $Re_d^{-4/3}$, and asymptotically approaches a constant value in the limit of high Re_d . The resistance coefficient can be evaluated by
106 these correlations with a fair degree of accuracy, see table 9. However, for high accuracy it is necessary to determine the value
107 experimentally for each grid and flow condition, this conclusion can be found in^{6,9}.

Mass flow [g/s]	50	75	106
Bulk velocity [m/s]	17	25	33
ξ experimental	0.600	0.611	0.614
ξ Groth and Johansson	0.621	0.609	0.601
ξ Roach	0.758	0.754	0.752

Table 9. Comparison of experimental results and grids correlations for WM Vide4Fil1 sample

108 Diamond grids pressure drop analysis

The diamond grids sample can be considered as a flow through a porous media configuration. Table 10 summarizes up the pressure drop coefficient obtained for the 2 types of diamond grids. A good approach to model this type of media is to use the modified Ergun equation¹²:

$$\xi = \frac{\alpha e \mu}{(1/2)\rho U_b \sigma} + \frac{\beta e}{(1/2)\sigma^2} \quad (4)$$

109 with $\alpha = \frac{A(1-\sigma)^2}{(\sigma^{3.6} * D_{eq}^2)}$ and $\beta = \frac{B(1-\sigma)}{\sigma^{3.6} D_{eq}}$, e the sample thickness, here chosen to be equal to d_c (see in diamond sample definition,
110 figure 3), σ the sample porosity and D_{eq} a characteristic medium length, here chosen to be equal to d_{pore} (see in diamond sample
111 definition, figure 3). Based on Gupte data base available in¹², the constants can be chosen as $A = 132.7$ and $B = 1.291$.

Mass flow [g/s]	50	75	106
Bulk velocity [m/s]	17	25	33
ξ experimental $d_c = 2.5\text{mm}$	110.4	117.5	177.6
ξ experimental $d_c = 4.5\text{mm}$	62.2	65.6	70.77
ξ Modified Ergun $d_c = 2.5\text{mm}$	81.8	80.42	80.33
ξ Modified Ergun $d_c = 4.5\text{mm}$	80.5	79.82	79.61

Table 10. Comparison of experimental results and grids correlations for diamond grids

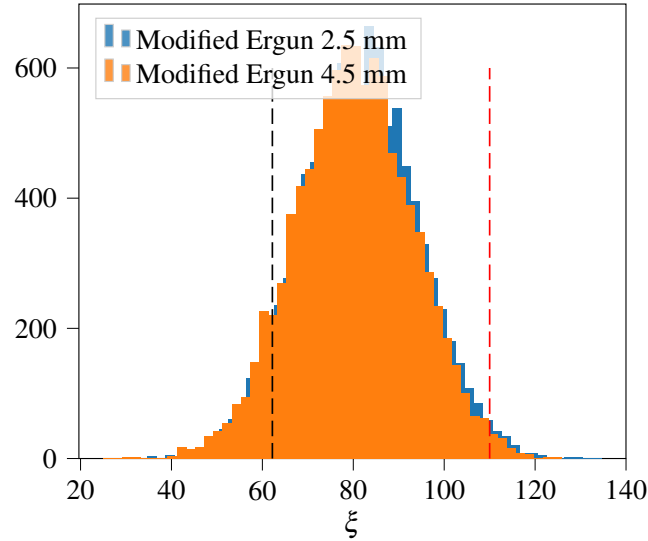


Figure 5. Normal distribution of Modified Ergun model of Diamond samples based on the model parameter distribution¹². The black and red vertical lines show the experimental value measured for $d_c = 4.5\text{mm}$ and $d_c = 2.5\text{mm}$, respectively.

Typically, this model should be calibrated on a large amount of samples to give some better results. Presently, in a first approach, the results are fairly good and the order of magnitude is respected even if the decreased of pressure drop between the two grids is not correctly estimated. Figure 5 shows the normal distribution of the modified Ergun model for the diamond samples, based on the geometric parameter of the grids. In Mac Donald et al.¹², the discrepancy between the experimental results and the model fit is available. The same distribution is plotted here in order to quantify this discrepancy while using only the geometric description of the sample. One can notice that the measured results on the diamond samples are in the distribution range which confirms the validity of the modified Ergun model.

Mean flow LDV results

Figures 6,7,8,9,10 and 11 present overall all mean flow results. Several remarks should be done on these mean fields. The measurement grids are globally quite coarse (36 points per plane). The spatial resolution is therefore not sufficient to describe the flow structures. However, the main trends can be identified. For the WM Vide4fil1 sample (figures 6 and 7), the effect of the wires can be seen on the first downstream position (35 mm). Rapidly, for the next plane position, one can notice that the upstream mean flow conditions seem to be recovered. For the diamond grid (figures 8,9), the incident flow which is measured 12 mm before the sample is highly impacted by a blockage effect due to the pressure loss which has a important impact on the meanflow profile. For the SCP case (figures 10 and 11) and the diamond grid (figures 8 and 9), the distance of the measurement planes downstream the samples seems not sufficient to recover a mean condition comparable to the incident flow. The turbulence measurements can give further information about the turbulence decay, this will be detailed in the next section.

Turbulence characterisation

For each plane, the median value of the turbulence rate is computed :

$$T_u = \int_y \int_z \frac{u_{rms}}{U} dydz \quad (5)$$

Downstream of a turbulence generating screen the turbulence intensity decays with a typical power-law decay. It has been found that the appropriate length for the decay is the mesh width M of the screen. The decay can be described by Batchelor and

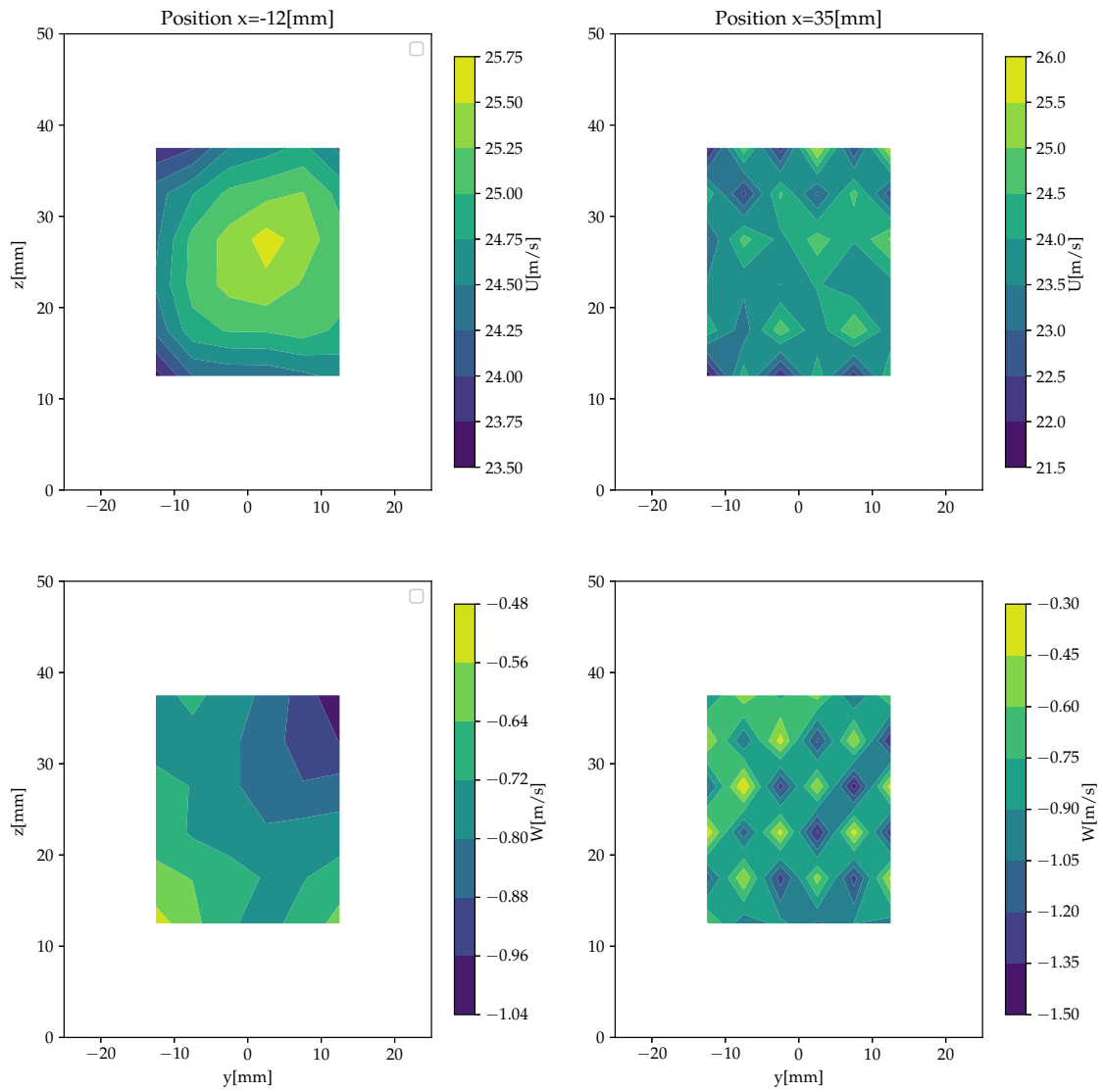


Figure 6. Mean velocity value for plane $x = -12$ mm and $x = 35$ mm. Vide4fill sample for a mass flow of 75g/s

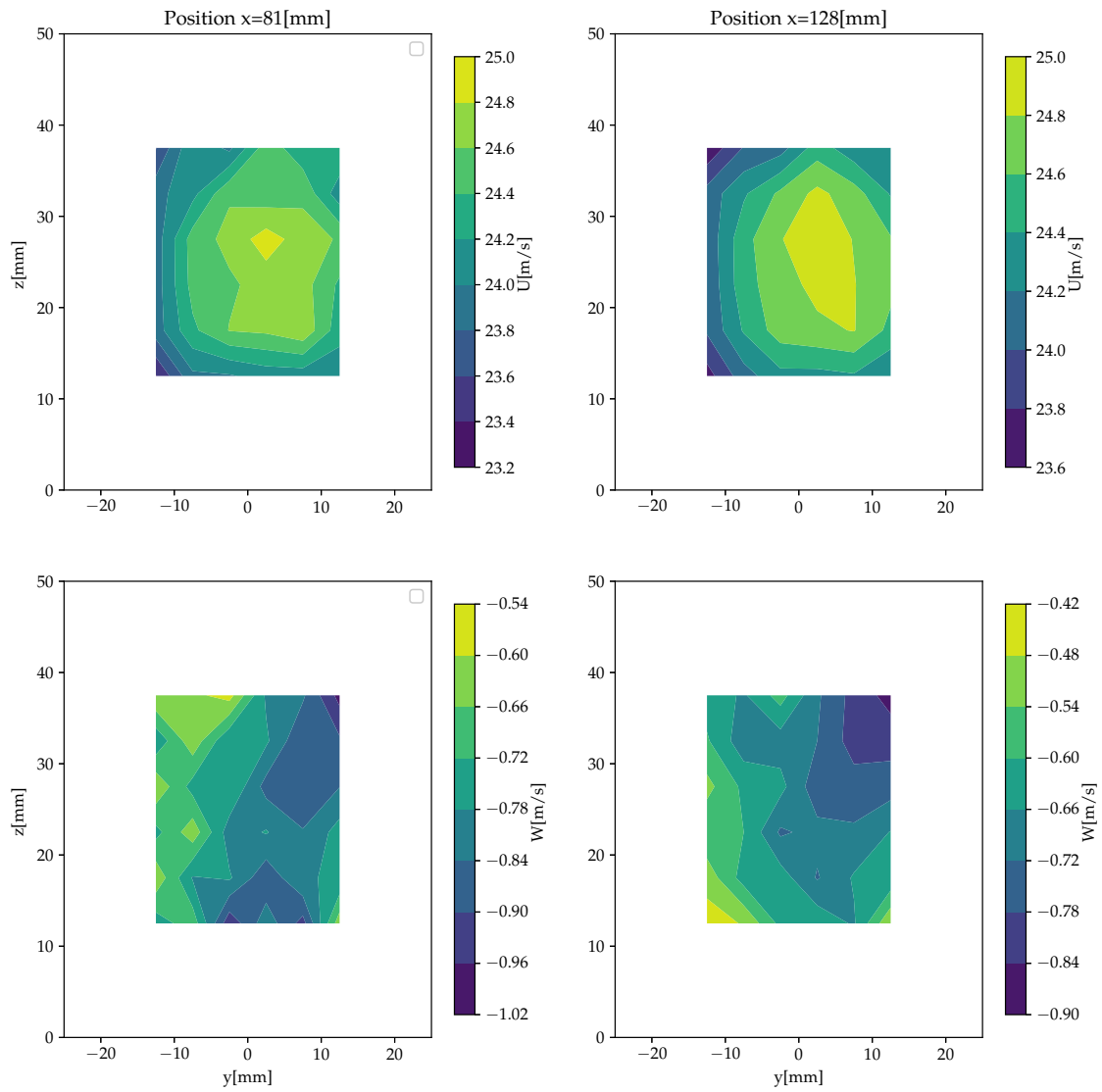


Figure 7. Mean velocity value for plane $x = 81$ mm and $x = 128$ mm. Vide4fil1 sample for a mass flow of 75g/s

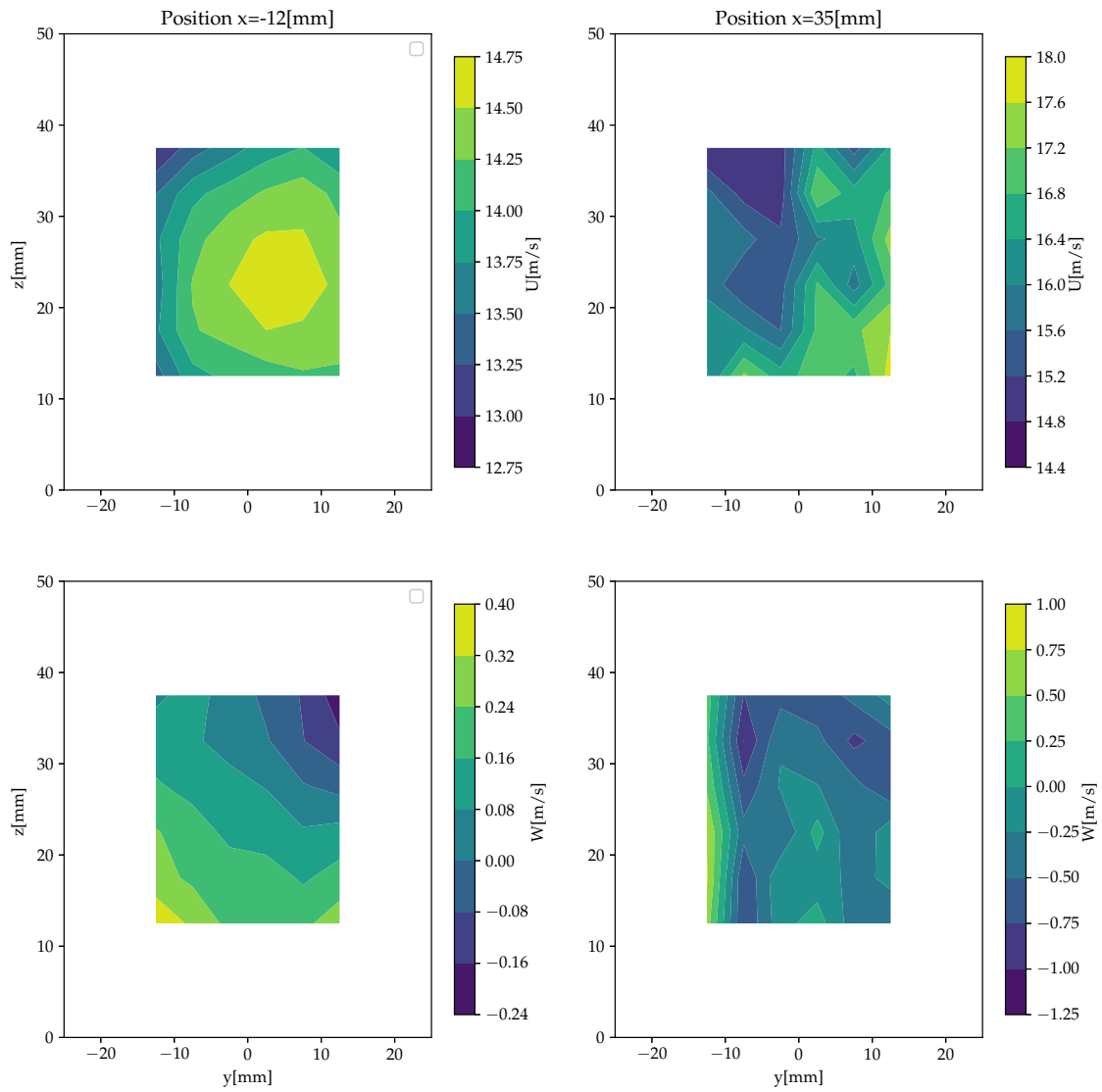


Figure 8. Mean velocity value for plane $x = -12$ mm and $x = 35$ mm. Diamond 4.5 mm for a mass flow of 75 g/s

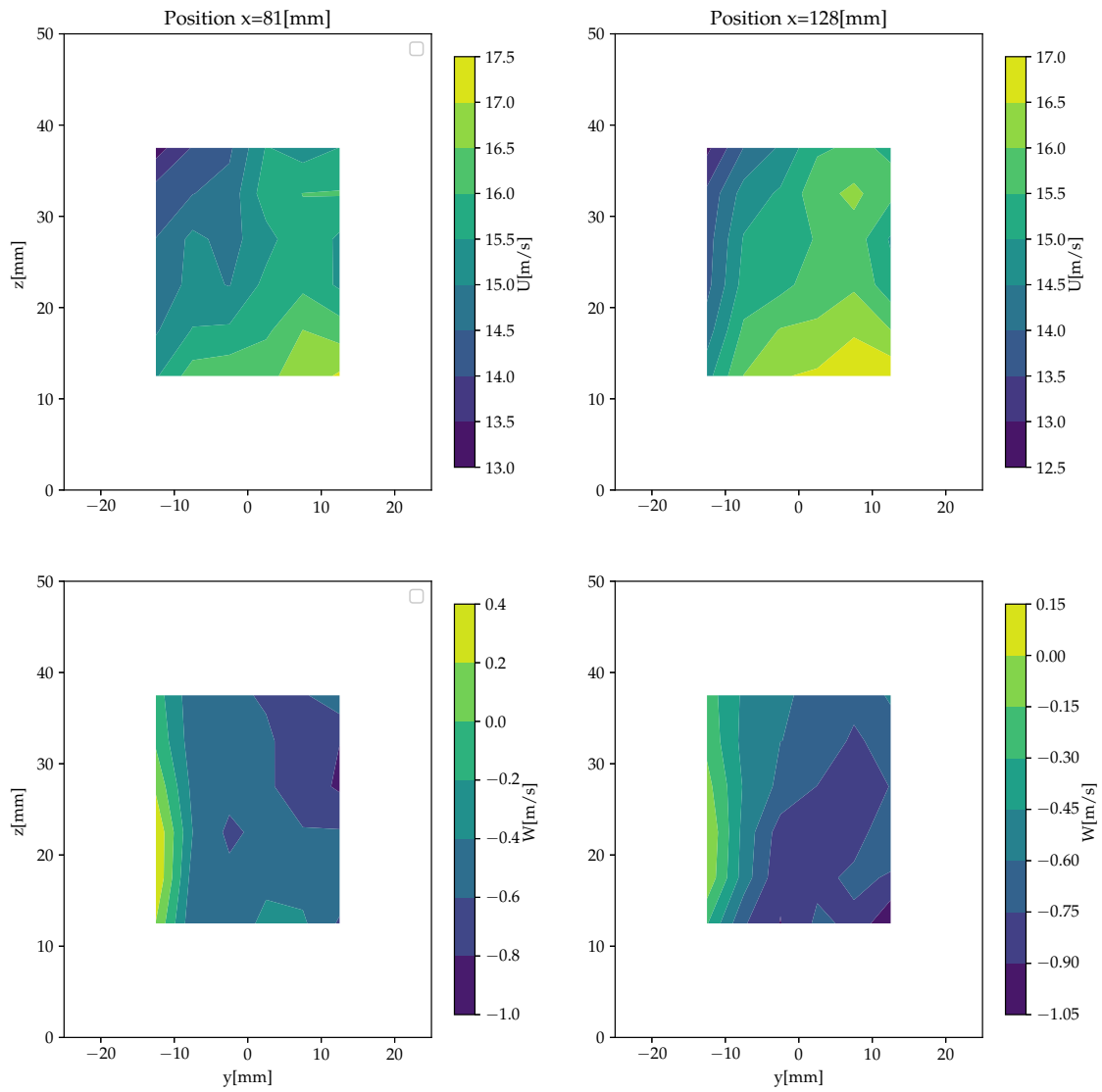


Figure 9. Mean velocity value for plane $x = 81$ mm and $x = 128$ mm. for Diamond 4.5 mm sample for a mass flow of 75 g/s

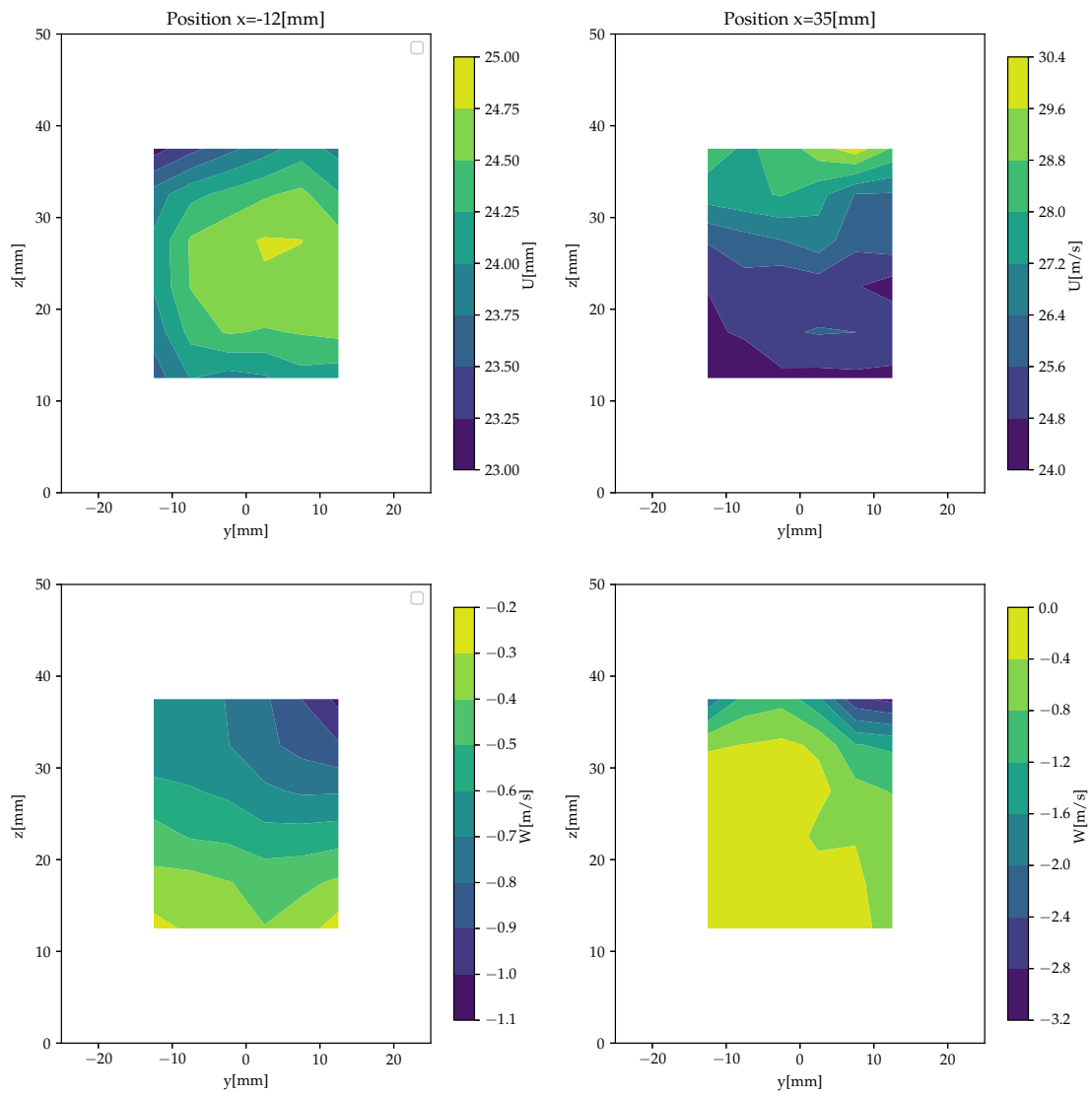


Figure 10. Mean velocity value for plane $x = -12$ mm and $x = 35$ mm. D2T3e2 sample for a mass flow of 75g/s

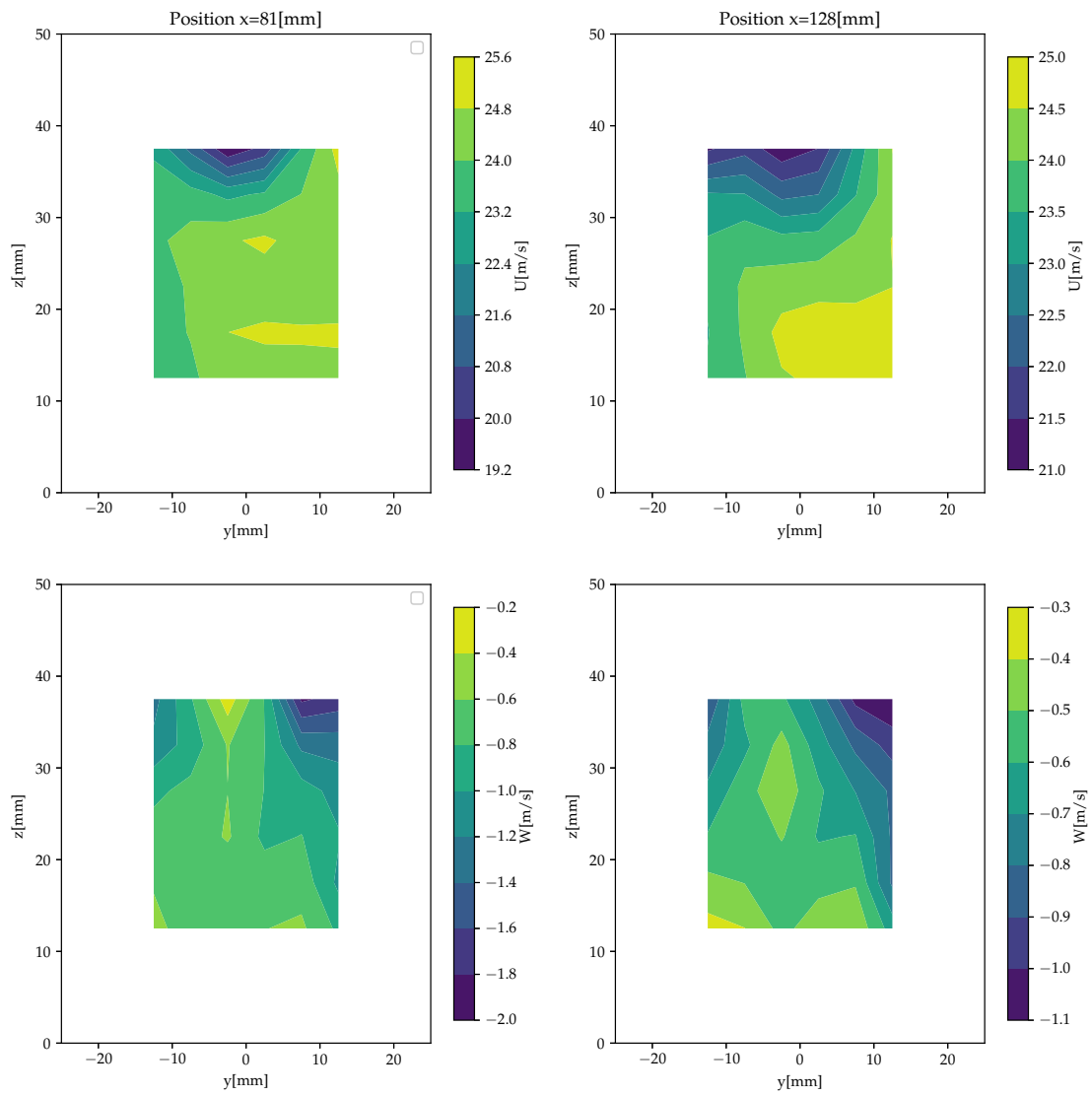


Figure 11. Mean velocity value for plane $x = 81$ mm and $x = 128$ mm. D2T3e2 sample for a mass flow of 75g/s

Townsend¹³ law:

$$T_u^2 = \left(\frac{urms}{U_b} \right)^2 = A \left(\frac{x - x_0}{M} \right)^b \quad (6)$$

130 where x_0 is a virtual origin of the screen (that is usually close to the actual position of the screen, in the present study it is the
131 actual position of the sample). The exponent b gives the decay rate and the constant A gives the level for a particular screen
132 and Reynolds number. An already identified problem is the large variation of the estimates of these coefficients, which is
133 often explained by an inconsistent determination procedure of the x/M interval chosen for the curve fit. However, one should
134 not exclude the initial scales generated by the grids as a candidate for the turbulence decay property as argued by several
135 authors. Kurian et al.⁶ proposed a systematic approach to characterize the turbulence, by means of energy spectra, characteristic
136 turbulence length scales, energy dissipation, kinetic energy decay rate etc., behind a set of grids with the feature of having
137 roughly the same solidity but different mesh and bar widths.

138 **Turbulence characterisation of the WM Vide4fil1**

139 The WM vide4fil1 sample is typically comparable with Kurian results especially with the mesh LT5 which is almost the
140 same type of mesh ; for WM vide4fil1, $M = 5\text{mm}$ and $d = 1\text{mm}$. The results for LT5 range from $A = [0.047; 0.068]$ and
141 $b = [-1.45; -1.42]$ whereas the results for WM Vide4fil1 appear to range from $A = [0.047; 0.068]$ and $b = [-1.5; -1.42]$,
142 categorized according to the reynolds number based on the mesh width M . Figure 12 shows the turbulence decay parameter
143 regression for the present data set. The turbulence decay is fairly comparable between the present study and Kurian et al. results.
144 Figure 13 presents the results from Kurian et al. and a comparison with the present results on WM Vide4fil1. In Kurian et
145 al., comparable samples have been tested and one can notice that the results obtained here with a different set up are really
146 consistent with the cited article.

147 **Turbulence characterisation of the D2T3e2**

For the D2T3e2 sample, the M value need to be defined. Roach¹⁰ proposes to use d_e which writes as

$$\frac{d_e}{D} = \frac{1}{\sigma^{1/2}} - 1 \quad (7)$$

148 as a turbulence length scale with $D = 2\text{mm}$ the holes diameter and $\sigma = 0.403$ the porosity. Figure 14 shows the parameter
149 regression with the present data set.

Roach proposes a correlation

$$Tu = 1.13 \left(\frac{x}{d_e} \right)^{-\frac{5}{7}} \quad (8)$$

150 which is superimposed to the present results. Note that the last plane gives a turbulence rate which is a little bit higher than the
151 turbulence rate at the previous planes. Nonetheless, the agreement is fairly good with Roach results (see figure 15).

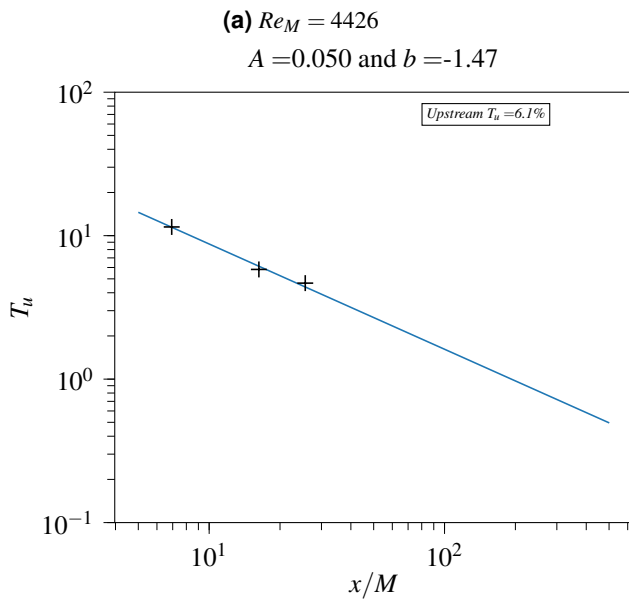
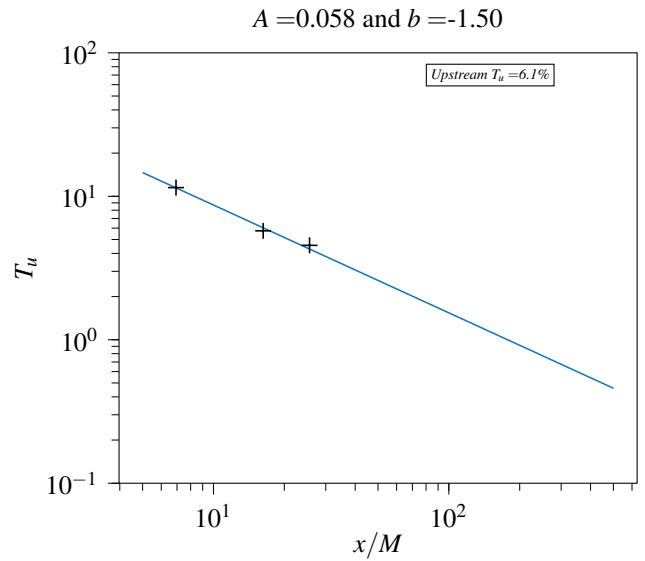
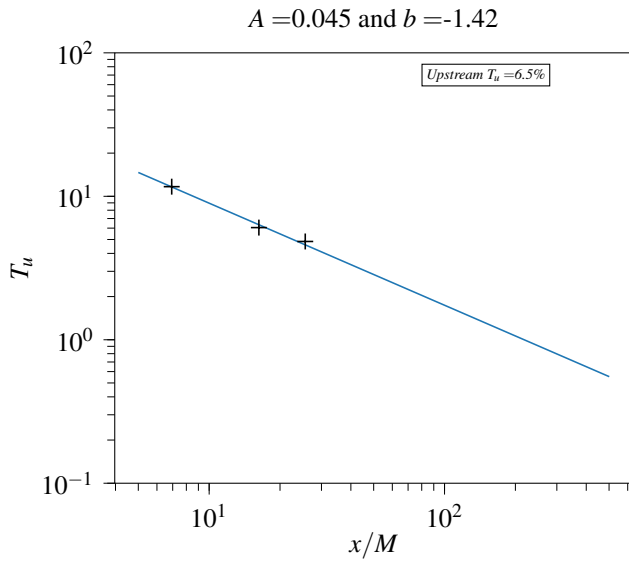


Figure 12. Turbulence decay regression for the WM Vide4fil1 sample

152 **Turbulence characterisation of the diamond sample**

153 Finally, figure 16 shows the turbulence parameter decay using $M = 4.5\text{mm}$ as a turbulence length scale for the diamond sample.
 154 Figure 17 presents the anisotropy of the turbulence for each samples (median value on each plane). Diamond and D2T3e2
 155 samples seems to be more isotropic than the WM Vide4fil1 sample.

156 Several fairing samples have been tested in the B2A test bench in order to create a data base of pressure loss for several
 157 mass flow conditions. Three different samples have been studied deeply in term of mean flow and fluctuating turbulence flow
 158 components based on LDV measurement enabling canonical configurations that can be reproduced numerically. Preliminary
 159 comparisons with correlations available in the literature show a quite good agreement with the present results.

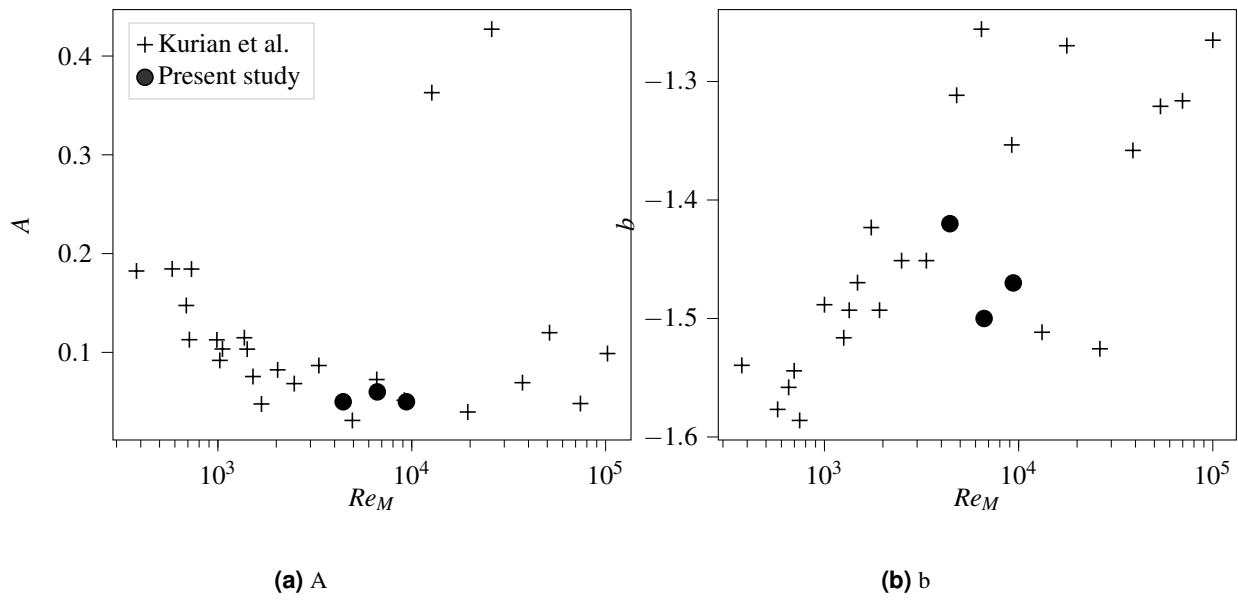
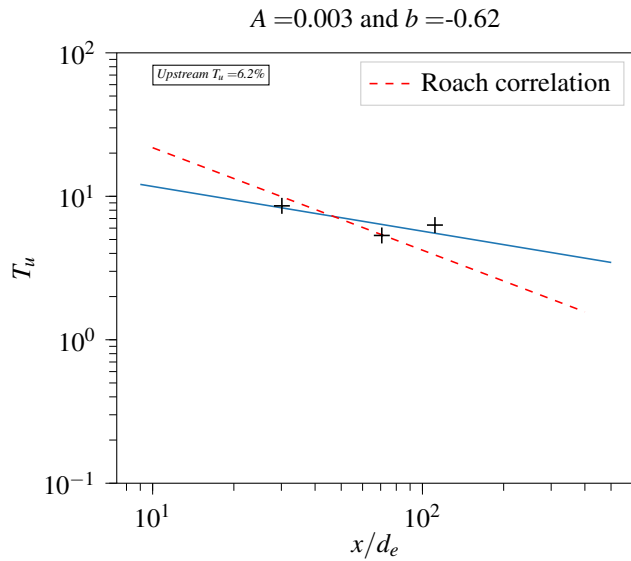


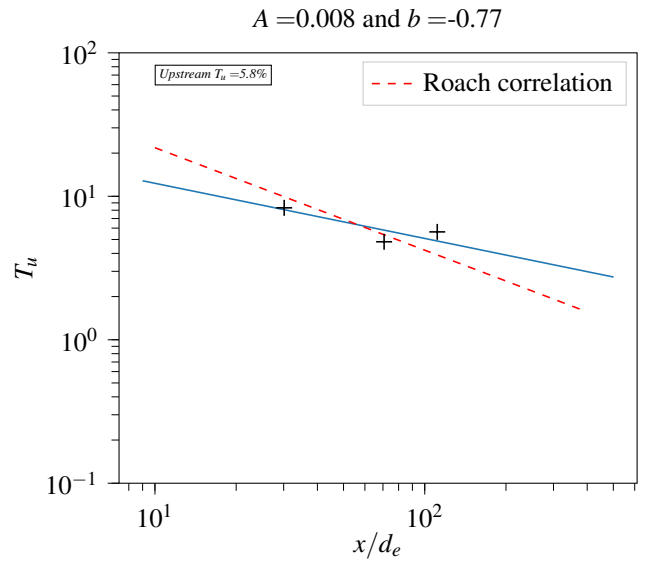
Figure 13. Batchelor and Townsend Turbulence decay for Vide4fil1 and Kurian et al.⁶

160 **Code availability**

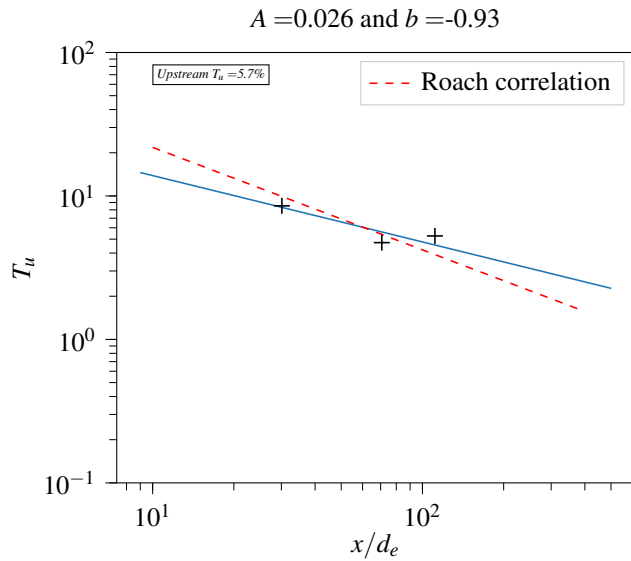
161 In order to read the "*.bin" files, a python code is provided in the zenodo deposit. The program "PSD_estimation.py" gives
 162 some routines to read and calculate the PSD of a given velocity component at a given point. Python required version is written
 163 as a comment in the python code.



(a) $Re_M = 4426$



(b) $Re_M = 6639$



(c) $Re_M = 9384$

Figure 14. Turbulence decay regression for the D2T3e2 sample

References

- 164 1. Khorrami, M. R., Lockard, D. P., Humphreys, W. M. & Ravetta, P. A. *Flight-Test Evaluation of Airframe Noise Mitigation*
 165 *Technologies*. <https://arc.aiaa.org/doi/pdf/10.2514/6.2018-2972>.
 166
- 167 2. Minotti, A., Simon, F. & Gantier, F. Characterization of an acoustic liner by means of laser doppler velocimetry in a
 168 subsonic flow. *Aerosp. Sci. Technol.* **12**, 398–407 (2008).
- 169 3. Lavieille, M. *Développement d'une méthode de mesure acoustique en écoulement rapide et chaud par Vélocimétrie Laser*
 170 *Doppler*. Ph.D. thesis, Université de Toulouse (ISAE) (2008).
- 171 4. Leon, O., Piot, E., Sebbane, D. & Simon, F. Measurement of acoustic velocity components in a turbulent flow using ldv
 172 and high-repetition-rate piv. *Exp. fluids* [10.1007/s00348-017-2348-4](https://doi.org/10.1007/s00348-017-2348-4) (2017).

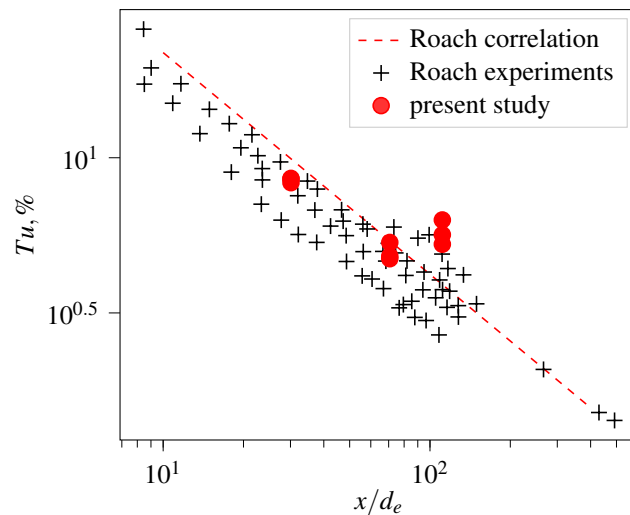
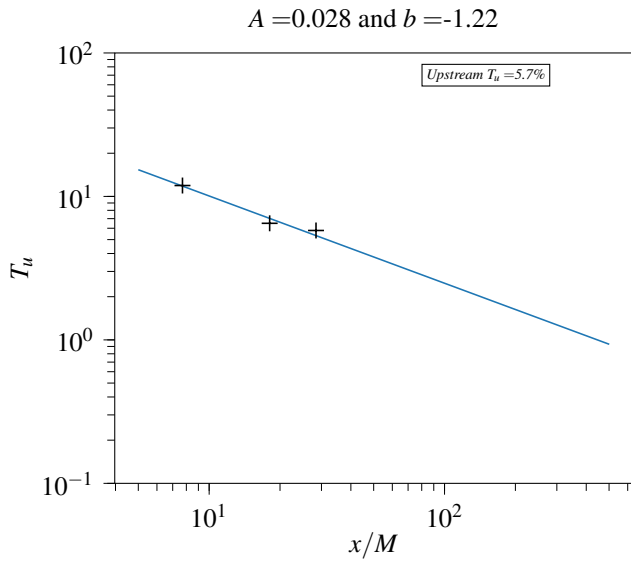
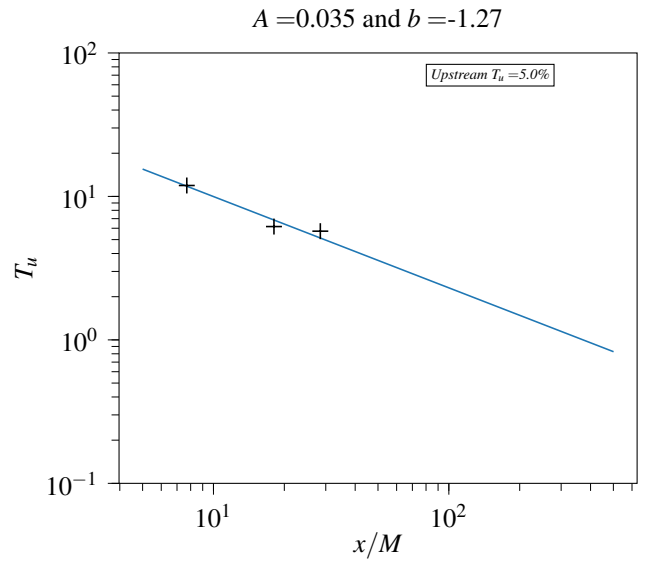


Figure 15. Roach data set and present study comparison

- 173 5. Micheli, F., Lavieille, M. & Millan, P. Assa, un outil de référence pour le traitement du signal en vélocimétrie laser. In
174 *Congrès Francophone de Techniques Laser* (Toulouse, 2006).
- 175 6. Kurian, T. & Fransson, J. H. M. Grid-generated turbulence revisited. *Fluid Dyn. Res.* **41**, 021403, [10.1088/0169-5983/41/](https://doi.org/10.1088/0169-5983/41/2/021403)
176 [2/021403](https://doi.org/10.1088/0169-5983/41/2/021403) (2009).
- 177 7. Morgan, P. High speed flow through wire gauzes. *The Aeronaut. J.* **63**, 474–475, [10.1017/S0368393100071467](https://doi.org/10.1017/S0368393100071467) (1959).
- 178 8. R.A. Pinker, M. H. Pressure loss associated with compressible flow through square-mesh wire gauzes. *J. Mech. Eng. Sci.*
179 **9**, issue 1, [10.1243/JMES_JOUR_1967_009_004_02](https://doi.org/10.1243/JMES_JOUR_1967_009_004_02) (1967).
- 180 9. Laws, E. M. & Livesey, J. L. Flow through screens. *Annu. Rev. Fluid Mech.* **10**, 247–266, [10.1146/annurev.fl.10.010178.](https://doi.org/10.1146/annurev.fl.10.010178.001335)
181 [001335](https://doi.org/10.1146/annurev.fl.10.010178.001335) (1978). <https://doi.org/10.1146/annurev.fl.10.010178.001335>.
- 182 10. Roach, P. The generation of nearly isotropic turbulence by means of grids. *Int. J. Heat Fluid Flow* **8**, 82–92, [https://doi.org/10.1016/0142-727X\(87\)90001-4](https://doi.org/10.1016/0142-727X(87)90001-4) (1987).
183 [https://doi.org/10.1016/0142-727X\(87\)90001-4](https://doi.org/10.1016/0142-727X(87)90001-4)
- 184 11. Groth, J. & Johansson, A. Turbulence reduction by screens. *J. Fluid Mech.* **1997**, 55 (1988).
- 185 12. Macdonald, I. F., El-Sayed, M. S., Mow, K. & Dullien, F. A. L. Flow through porous media—the ergun equation revisited.
186 *Ind. & Eng. Chem. Fundamentals* **18**, 199–208, [10.1021/i160071a001](https://doi.org/10.1021/i160071a001) (1979). <https://doi.org/10.1021/i160071a001>.
- 187 13. Batchelor, G. K. & Townsend, A. A. Decay of isotropic turbulence in the initial period. *Proc. Royal Soc. A* **193**,
188 [10.1098/rspa.1948.0061](https://doi.org/10.1098/rspa.1948.0061) (1948).



(a) $Re_M = 4426$



(b) $Re_M = 6639$

Figure 16. Turbulence decay regression for the Diamond Sample

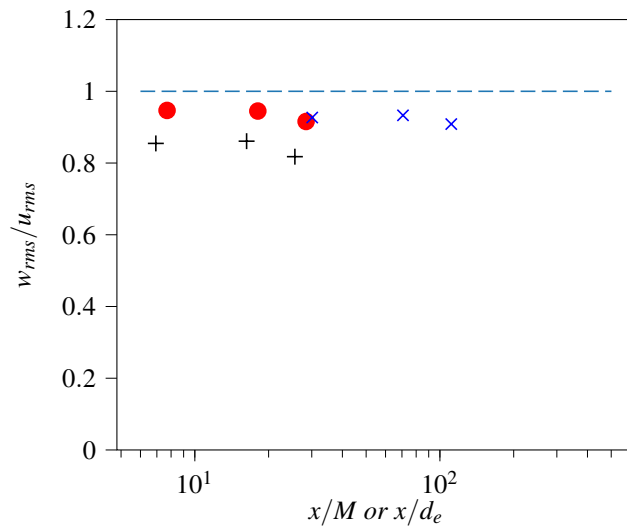


Figure 17. Turbulence anisotropy for WM vide4fil1 (black mark), D2T3e2 sample (red mark) and Diamond sample (blue mark), mass flow 75 g/s.